



Quantitative mineralogy for facies definition in the Marcellus Shale (Appalachian Basin, USA) using XRD–XRF integration

Brittany N. Hupp*, Joseph J. Donovan

Department of Geology & Geography, West Virginia University, 330 Brooks Hall, Morgantown, WV 26506-6300, USA

ARTICLE INFO

Article history:

Received 5 March 2018

Received in revised form 27 April 2018

Accepted 28 April 2018

Available online 6 May 2018

Editor: Dr. J. Knight

Keywords:

Clay minerals

Marcellus Shale

Mineralogy

Mudrock

X-ray diffraction

X-ray fluorescence

ABSTRACT

Determining the mineralogy of mature sedimentary rocks, particularly mudrock, often defaults to qualitative or semi-quantitative methods due to difficulties in correctly quantifying multiple unknown mineral phases. Constraining mineral abundances is particularly difficult in shale due to preferred mounting orientation of common phyllosilicate phases, commonly leading to overestimation of clay minerals and mica. We introduce a quantitative approach to constraining mineralogy within mudrock by integrating x-ray diffraction (XRD) and x-ray fluorescence (XRF) data sets collected on splits of the same samples. The technique involves partitioning XRF cation concentrations into XRD-identified silicate, carbonate, and sulfide phases, then estimating quartz by XRF SiO₂ balance. This method is applied to an example dataset from the economically significant Marcellus Shale (Middle Devonian, Appalachian Basin, USA). Conventional reference-intensity ratio (RIR) interpretation identified nine mineral phases (quartz, muscovite, illite, pyrite, chlorite, albite, calcite, dolomite, and barite). Their abundances were then re-estimated using more highly accurate XRF-derived elemental concentrations with stoichiometry from the identified XRD reference phases. XRF Al₂O₃ was used to corroborate the calculated XRD–XRF results for quality control. Errors in relevant XRF concentrations can be quantified, though not the assumptions in how they are employed; nonetheless, the resulting XRD–XRF mineralogic abundances by this procedure are thought to be more accurate than RIR and to remove preferred-orientation bias induced that causes overestimation of clay minerals and mica and underestimation of quartz and other phases. Cluster analysis of the XRD–XRF results identified four mineralogical facies that provide insight into potential primary depositional controls on organic-matter preservation within the Marcellus Shale. This XRD–XRF integration method provides a general framework for estimating mineralogy quantitatively in mudrocks, although dataset-specific adjustments to the method may be required for different mineralogical suites.

© 2018 Elsevier B.V. All rights reserved.

1. Introduction

Mineral identification by x-ray diffraction (XRD) may be undertaken using either qualitative (e.g., identification), semi-quantitative, or quantitative methodologies, each of which has its own applications, limitations, and pitfalls (Klug and Alexander, 1974). Simple identification can generally be accomplished with ease for single mineral phases and, with more difficulty, for mixtures of two or more phases. Sources of error in this determination include variable composition and/or structure of unknowns with respect to reference phases (Srodon et al., 2001), inadequate sample preparation (Jenkins, 1989), and unknowns occurring in low concentration within the mixture. All of these problems, and several others, are compounded in semi-quantitative and, especially, quantitative analysis of mineral composition of rocks and soils.

One application in which quantification by XRD poses a major challenge is the mineralogy of mudrocks, particularly that of shale. These rocks are deposited in marine, marginal marine, or lacustrine settings and may reflect provenance of local sediment/orogenic sources and intrabasinal sedimentation as well as the effects of diagenesis and/or metamorphism (Saupe and Vegas, 1987; Potter et al., 2005; Zhou and Keeling, 2013). As a result, mineralogical suites in such strata are commonly diverse and can contain multiple phases of clay-mineral, mica, carbonate, aluminosilicate, and sulfide groups, as well as quartz and organic matter. In addition to the large number of phases, another obstacle to quantification is the preferred orientation of, especially, phyllosilicate phases. Upon mounting, some minerals tend to align according to their crystallographic orientation including gypsum (Grattin-Bellew, 1975) and, especially, clays and micas (Braun, 1986; Kolka et al., 1994; da Silva et al., 2011). While various methods have been described to minimize preferred orientation (Poppe et al., 2001), it is common to observe discrepancies between both quantitative and semi-quantitative XRD concentrations and accurately analyzed elemental chemistries (Hillier, 2000; Raven and Self, 2017). Given that clay

* Corresponding author at: Department of Geoscience, University of Wisconsin-Madison, 1215 W. Dayton St., Madison, WI 53706-1692, USA.
E-mail address: bhupp@wisc.edu (B.N. Hupp).

minerals and micas may comprise 50% by weight or more of black-shale mineral content, to accurately quantify mineralogy of such rocks requires dealing with the preferred-orientation problem.

One such approach, which has been applied to quantify shale mineralogy, is integration with elemental chemistry from other analytical techniques. The most common method for such determination in rocks and soils is X-ray fluorescence (XRF). As for XRD, XRF may be used for qualitative, semi-quantitative, or quantitative determinations, depending on factors including the instrument employed, whether and how calibration is performed, sample mounting, and analytical care in counting statistics and matrix correction. Quantitative XRF analysis is generally performed using wavelength-dispersive (WDS) rather than energy-dispersive (EDS) spectrometry (Zwicky and Lienemann, 2004). A homogeneous sample of sufficient thickness is required to attenuate all primary x-rays from the instrument as well as standards of concentration known to high accuracy for calibration. XRF-determined concentrations of major elements are conventionally reported as oxides for major ions, including Na, K, Ca, Mg, Fe, Mn, Si, Al, Ti, and P, generally summed by convention to 100% of the total mass concentration of the sample.

In principle, these oxide concentrations might be used to at least estimate the underlying mineralogy. Indeed, in igneous petrology, elemental-oxide concentrations have been used to directly estimate mineralogy by the so-called Cross, Iddings, Pirsson, and Washington (CIPW) normative method that relies on a number of a priori assumptions and “rules of thumb”, summarized in Kelsey (1965). However, in the sedimentary petrology of shales, a heuristic basis is lacking for such a unique normative procedure; simply too many possible combinations of silicates, clay minerals, and micas exist for a “rule of thumb” approach to be viable. In addition to the complexity of the mineral assemblages, an additional problem involves the fact that such sediment often contains organic matter and other amorphous phases (e.g., iron oxides), causing potentially significant differences in mass balance between XRD and XRF results.

A number of previous investigations have used XRF either to aid in corroboration of XRD identifications or to support quantification of XRD results. Combinations of XRD and XRF microprobe mapping with other analytical tools (e.g., x-ray absorption near-edge spectroscopy, Fourier Transform Infrared spectroscopy, and Raman spectroscopy) have been used to differentiate carbonate species at low concentrations (Blanchard et al., 2016) and evaluate diagenesis (Piga et al., 2011). Synthesis of quantitative laboratory-based XRD and XRF results was used to evaluate the accuracy and precision of a portable XRD on known mixtures for application to the mineralogy of hydrothermal systems (Burkett et al., 2015). XRD-XRF data has also been used to assess weathering rates and subsequent soil formation (Ferrier et al., 2010), metallurgical ores (Hausen and Odekirk, 1991), and synthetic mixtures (Schorin and Carías, 1987). It has also been suggested as a technique with multiple industrial applications (Loubser and Verryn, 2008). Despite these studies, little has been done to support quantifying mineralogy for fine-grained sedimentary rocks (Medrano and Piper, 1991).

The purpose of this investigation is to develop a normative-style procedure integrating XRD and high-accuracy WDS-XRF elemental-oxide chemistries to produce quantitative mineral abundances for shales. Particular emphasis is placed on mineralogy of the Marcellus Shale (Devonian) of the Appalachian Basin, USA. This will involve development of rule-based partitioning of XRF elemental masses according to XRD observations to estimate mineral concentrations, as well as some check on error between calculated and observed elemental mass balance. The correspondence between mineral abundance by a conventional semi-quantitative XRD-based method and this integrated XRF-XRD method will be examined.

2. Geologic framework

Samples for this study were collected from a gas well in northeastern West Virginia, USA, from the Middle Devonian Marcellus Shale (Fig. 1).

Within the study area, the Marcellus Shale is a ~30 m thick, heterogeneous formation dominated by gray to black, thinly laminated, organic-rich shale. Bentonite layers, known as the Tioga Ashes, are found interbedded within the basal part of the Marcellus Shale (Roen and Hosterman, 1982; Dennison and Textoris, 1988; Ver Straeten, 2004). The Marcellus Shale is overlain by the Middle Devonian (Givetian) Mahantango Formation and underlain by the Onondaga Limestone (Dennison and Hasson, 1976; Soeder et al., 2014) (Fig. 2). The Marcellus Shale and Mahantango Formation make up the Hamilton Group. Contacts above and below the Marcellus Shale are gradational and marked by a change in gamma-ray response, indicating a transition from organic-rich to organic-poor facies (Soeder et al., 2014; Hupp, 2017).

The Marcellus Shale was deposited from 394 to 389 Ma during the Acadian Orogeny within the Appalachian Basin of eastern North America (Parrish, 2013). At this time, oblique collision of Avalonia with the eastern margin of Laurentia formed the Acadian foreland basin in which the fine-grained sediments of the Marcellus Shale were deposited (Ettensohn, 1985; Hibbard et al., 2010; Ver Straeten, 2010; Lash and Engelder, 2011; Ettensohn and Lierman, 2013). Paleogeographic reconstructions indicate that the Acadian basin was located approximately 20–30° south of the paleoequator. The Marcellus Shale of West Virginia provides a record of distal sedimentation within the epeiric Kaskaskia Sea during a tectonically active period.

Marcellus Shale lithology is dominantly shale that reflects organic-rich pelagic intrabasinal and clastic extrabasinal sedimentation under anoxic bottom-water conditions. Mineralogy in the Marcellus Shale is diverse (Hupp, 2017), with total-organic carbon (TOC) concentrations as high as 15% (Wang and Carr, 2013; Enomoto et al., 2014; Yu, 2015). In recent years, it has been the focus of substantial economic interest due to its hydrocarbon production potential. Massive organic carbon burial associated with this unit has been cited as a key influence in the global cooling that occurred from Eifelian into Givetian time (Ellwood et al., 2011). The high content of organic carbon and intrinsic diversity of mineralogy make the Marcellus Shale an ideal candidate for this study.

3. Materials and methods

3.1. Sampling and sample preparation

Fifty-five samples were collected by diamond-drill coring through the Marcellus (API # 47061017050000) in Monongalia County, West Virginia (Fig. 1). Horizontal side-wall mini-core samples were taken at intervals between 0.5 (0.15 m) and 8.5 ft. (2.60 m; average 1.7 ft., 0.52 m) between depths of 7455.0 ft. (2272.3 m) and 7556.2 ft. (2303.1 m) below land surface. Each 25-mm-diameter side-wall plug was 11 to 16 cm long, of which the outer ends were used for geochemical characterization. The two end pieces were 1.5 to 6 cm long and together weighed 10–50 g. Each sample was crushed into ~1 cm fragments, then pulverized for approximately 4 to 6 min using a Spex® Model 5100 steel shatterbox. This grinding duration was observed to produce powders with >65% of grains smaller than 100 µm. These powders were then split into two aliquots, one to be pressed using a hydraulic ram into Chemplex™ pellets for XRD and the other for XRF and organic/carbonate analysis.

3.2. X-ray diffraction analysis

Chemplex-mounted pressed-pellet sample disks were analyzed using a PANalytical X'Pert Pro™ X-ray Diffractometer with a CuK α source at 2 θ angles from 5° to 75° and a step time of ~12 s per degree (total scan time 13.5 min). X-rays were focused through a 20-mm slit onto an Xcelerator™ detector. Samples were irradiated on a stage spinning at 1 revolution/s, with divergence and antiscatter slit angles of 0.5° and 1°, respectively. The x-ray beam was operated at voltage 45 kV and

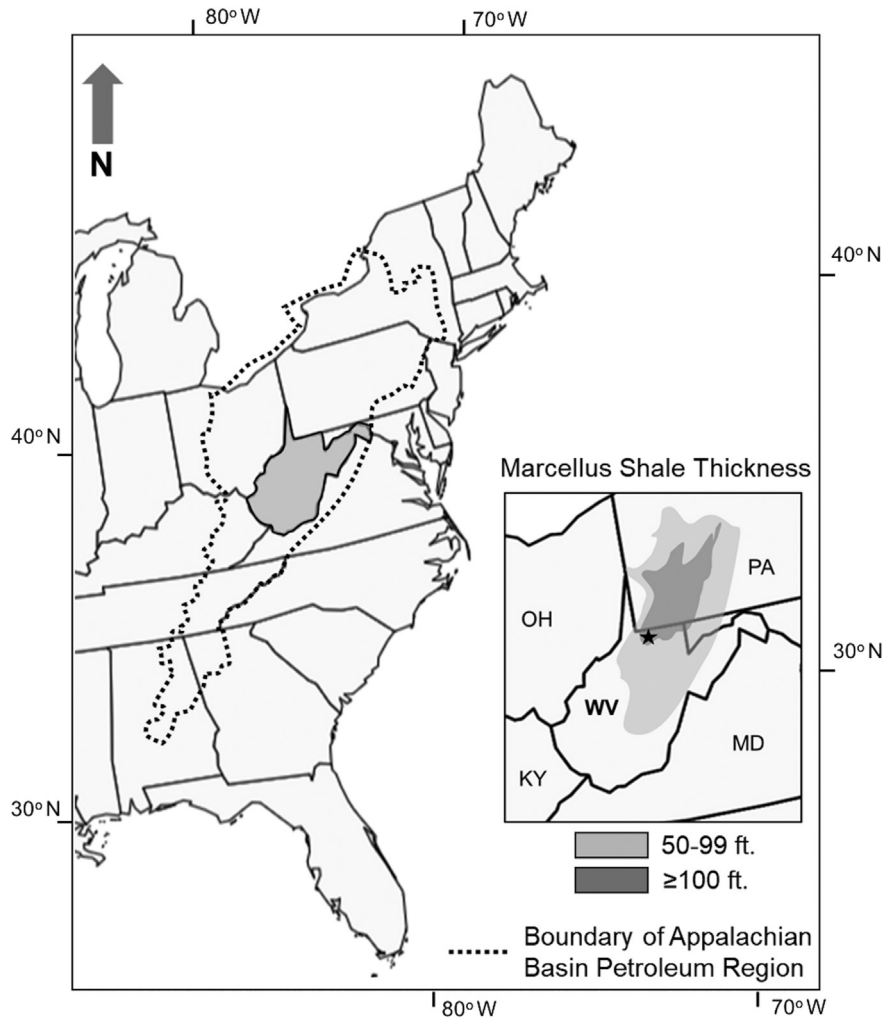


Fig. 1. Map showing the location of the study area with the state of West Virginia marked in dark gray (large map). Location of the sampled well (star) and the approximate thickness of the Marcellus Shale in the central Appalachian Basin region shown in the small inset. (50–99 ft. = 15.2–30.2 m; 100 ft. = 30.5 m) Thickness data from Milici and Swezey (2014).

current 40 mA. Mineral phases were qualitatively identified using the PDF2 reference library (ICDD, 2004) and PANalytical X’pert HighScore Plus©. Percentages were estimated semi-quantitatively using the

reference-intensity ratio (RIR) matrix-flushing method (Chung, 1975a, 1975b) based on selected PDF2 reference samples chosen for each mineral phase (Table 1). For consistency, the same reference phases were

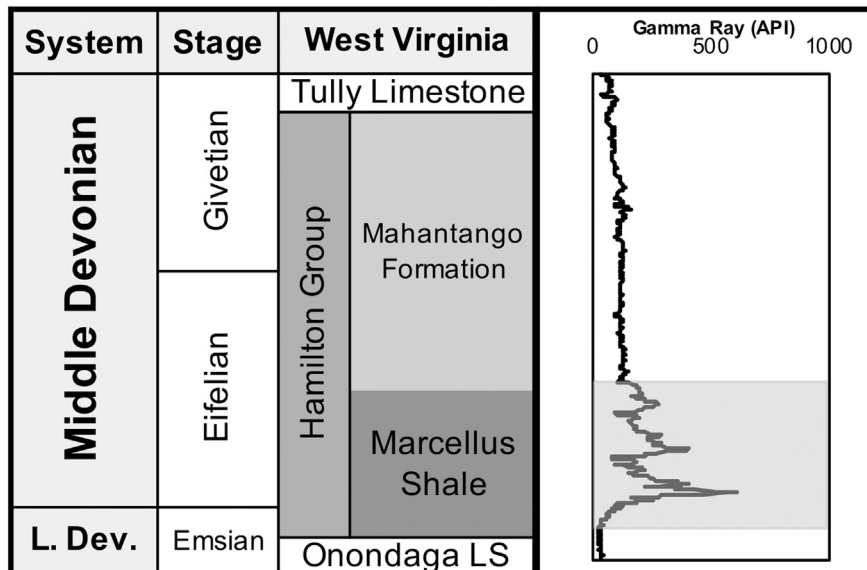


Fig. 2. Stratigraphic column showing regional Appalachian stratigraphy with accompanying gamma-ray log from the sampled well.

Table 1
Mineralogical information from the PDF2 reference library (ICDD, 2004).

Mineral name	PDF2 Reference Code	Chemical formula	Gram formula wt.	RIR	Diagnostic peak	I/I ₀ intensity
Albite	00-009-0466	NaAlSi ₃ O ₈	262.2	2.1	3.196 Å (002)	100
Barite	01-089-7357	BaSO ₄	233.3	2.78	3.044 Å (021)	100
Calcite	01-083-0578	CaCO ₃	100.0	3.21	3.035 Å (104)	100
Chlorite	01-089-2972	Mg _{2.5} Fe _{1.65} Al _{1.5} Si _{2.2} Al _{1.8} O ₁₀ (OH) ₈	599.9	1.06	7.08 Å (001)	84.3
Dolomite	01-073-2409	CaMg(CO ₃) ₂	184.0	2.42	2.899 Å (104)	100
Muscovite	01-082-0576	KAl ₂ (AlSi ₃)O ₁₀ (OH) ₂	380.3	0.38	9.96 Å (001)	64.1
Pyrite	01-071-1680	FeS ₂	119.9	0.89	2.708 Å (200)	100
Quartz	00-005-0490	SiO ₂	60.1	3.6	3.34 Å (101)	100

employed for each mineral in all samples so that RIR concentrations were determined consistently between samples. The concentrations were calculated on a weight-percent basis of the total inorganic (crystalline) fraction of the sample, under the assumption that amorphous phases present, aside from organic matter, made up little to none of the bulk sample. The sources of largest potential error from this XRD analysis are the detection limits of the diffractometer and mis-identification of peaks.

3.3. X-ray fluorescence analysis

XRF analysis was performed on the second aliquot of powders for all 121 samples to quantify both major, minor, and trace elements. A sample size of 1.0 g of each powder was fused into 15 mm glass disks and analyzed for approximately 3 h using a Thermo ARL PerformX™ X-ray Fluorescence Spectrometer with a programmable aperture to measure a suite of 40 elements. Prior to fusion, all powders were analyzed by serial loss on ignition (LOI) at temperatures of 600 °C and 900 °C, to quantify organic matter and carbonates. The powders were heated overnight in glass crucibles within a programmable furnace.

To create the glass disks for analysis, 1 part powder and 2 parts fusion flux were combined in a vortex mixer and fused in a Merson grade UF-4S graphite crucible in an electronic furnace at 1000 °C. Following first fusion, disks were cleaned, reground to a fine powder in a WC ring-mill and fused again at 1000 °C. Final glass disks are ultrasonically cleaned in ethanol prior to XRF analysis. Some elements are volatile during fusion and can lead to minima reports of Cl, S, Br, and As. Beads were then analyzed at an accelerating voltage of 45 kV at 45 mA. Crystalline material was kept at analysis temperatures of 43 °C and near constant pressure at 2.0 Pa. Accuracy was tested by running multiple certified reference standards simultaneously as unknowns (USGS AGV-2, BCR-2, BHVO-1, G-2, W-2, SDO-1, SCo-1, and STM-1). Precision and reproducibility were monitored by including at least one replicate sample for every ten analyzed. Errors associated with XRF analyses are summarized in Table 2.

XRF concentrations were determined on the LOI 900 °C ashed samples and thus are on a weight-percent basis of the total inorganic fraction. Significant alteration of some minerals may have likely occurred during ashing, such as dehydration of clays and decarbonation

of carbonate minerals (calcite and dolomite). However, these losses would have no bearing on the calculated XRD-XRF mineralogies, which were based on each mineral's XRD-determined stoichiometry and reference cation concentrations, only.

3.4. Petrographic analysis, scanning electron microscopy, and TOC estimation

Twenty-five thin sections from the Marcellus Shale were used for petrological analysis and mineralogical phase expression using a Nikon ECLIPSE LV100N POL polarizing microscope. Thin sections were prepared from selected 25-mm diameter sidewall plugs from the same set of samples as those used for XRF and XRD analysis. All thin sections were ground to the standard thickness of 30 µm.

Scanning electron microscopy was performed on some of the Marcellus Shale thin sections using a Hitachi S-4700 SEM. The non-Au-coated thin sections were examined under secondary electron mode with an accelerating voltage of 5.0 kV.

Mineralogical results are compared to a uranium-predicted total organic carbon log for the MIP-3H well. Total organic carbon was directly measured on samples from this well using a source rock analyzer (SRA) (Paronish, 2018). Results from both these analyses were then used to calibrate an existing gamma-ray log and create a continuous uranium-predicted total organic carbon log.

4. Results

4.1. RIR XRD mineralogy

Nine mineral phases were positively identified by XRD in the Marcellus samples: quartz, muscovite, illite, clinocllore (a.k.a. chlorite), pyrite, albite, calcite, dolomite, and barite (Table 1; Supplemental Table 1). Powders analyzed by XRD were not treated to remove organic matter; however, organic matter does not refract X-rays according to Bragg's Law and thus these XRD results only reflect crystalline mineral phases, therefore expressed as a percentage of the crystalline fraction only (Supplemental Table 1).

Because the XRD patterns for illite and muscovite are essentially indistinguishable, the RIR-identified percentages for these phases are

Table 2

Errors associated with XRF analysis including % error among each of the standards run as unknowns as well as the mean error deviation and standard error of the mean deviation for the pool of replicate samples.

Certified reference materials	n	Statistic	units	SiO ₂	Al ₂ O ₃	FeO*	MgO	CaO	Na ₂ O	K ₂ O	Ba	Sr
AGV-2	1	absolute error ([sample-standard]/sample)	%	0.30	1.25	-0.21	1.48	0.39	0.99	0.08	1.68	-0.83
BCR-2	1	absolute error ([sample-standard]/sample)	%	-0.13	-0.04	-0.15	-0.79	-0.72	-1.86	-0.74	0.67	-1.88
BHVO-2	1	absolute error ([sample-standard]/sample)	%	0.30	-0.86	0.54	0.08	0.51	-0.44	-1.09	4.23	-0.96
G-2	1	absolute error ([sample-standard]/sample)	%	0.09	1.14	-2.37	-0.69	0.20	-0.96	0.60	0.89	0.53
SCo-1	1	absolute error ([sample-standard]/sample)	%	0.44	1.77	-1.67	3.26	1.72	-3.49	-0.55	-3.10	-0.90
STM-1	1	absolute error ([sample-standard]/sample)	%	0.93	-0.04	-1.40	-22.84	-8.15	1.41	0.93	-2.20	-1.36
W-2	1	absolute error ([sample-standard]/sample)	%	0.05	-0.16	1.93	0.44	0.28	-1.73	-1.03	3.02	-0.81
<i>Sample Replicates</i>												
samples	3	sample mean error deviation	%	0.49	0.96	-1.81	-6.76	-2.08	-1.01	0.33	-1.47	-0.58
samples	3	sample standard error of mean deviation	%	0.24	0.53	0.29	8.12	3.07	1.41	0.45	1.21	0.57

combined (e.g., “illite + muscovite”) and their identification employed a single reference phase (PDF2 01–082–0576). Petrographic evaluation of several Hamilton Group photomicrographs suggests the possible co-existence of both phases (Hupp, 2017). Illite could not be clearly visually identified in the shale matrices; however, larger muscovite grains were identifiable as euhedral, highly birefringent, elongate (commonly ~50 μm) grains (Fig. 3).

The RIR results are calculated to the nearest unit wt% and sum to $100\% \pm 1\%$. This analysis requires that each identified mineral's reference phase have a calculated RIR value. Estimation of error associated with RIR concentrations of unknown sample mixtures is not straightforward. Hillier (2000) found ranges of relative error (i.e., error divided by concentration) from a few percent to as high as 100% using RIR, with the higher errors associated with minerals at lower, near-detection-limit concentrations. Direct estimation of error for RIR-determined mineralogy in this study was not attempted.

4.2. XRF elemental chemistry

Results of quantitative XRF analysis are shown in Supplemental Table 2 for elemental oxides (SiO_2 , Al_2O_3 , FeO , MgO , CaO , Na_2O , K_2O , BaO , SrO , and SO_3) in wt% of the sample fraction comprised of these elements. Weight % loss at LOI 600 $^\circ\text{C}$, the mass of volatilized organic matter, and LOI 900 $^\circ\text{C}$, the mass volatilized from decarbonation of carbonate minerals are also included within Supplemental Table 2. This mass basis was employed to mirror the basis for the XRD estimates as closely as possible. Barium (on average > 1.05%) and strontium were included in the oxide set as they were both in high concentration in a trace-element suite run on the same samples. The strong correlation ($R^2 = 0.979$; Fig. 4) observed between the more elevated XRF BaO and SrO concentrations suggest they may be present in the same mineral phase. Ba reaches high concentrations (>15% as BaO) in one sample at 7544.4 ft. Barite was identified by XRD in some, but not all, XRD samples, with variable BaO concentrations. In the other samples, barite is either below detection, or not present, while Ba may also occur in other phases, presumably carbonates. SrO is generally one or more orders of magnitude lower than BaO in molar concentration and, because strontian mineral phases are absent or non-detectable, there is a good possibility that where barite is identified, it is strontian, similar to observations by other investigators (He et al., 2014). The average mass ratio

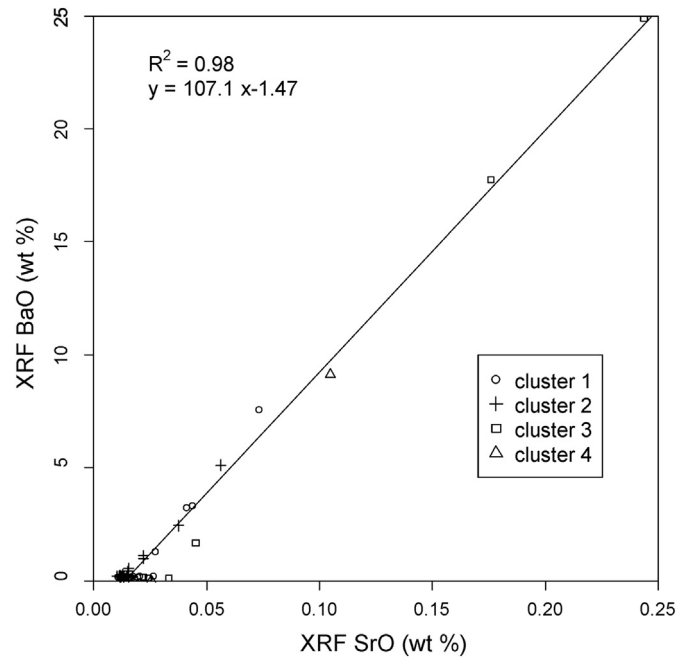


Fig. 4. Plot of XRF-determined BaO vs SrO in Marcellus samples, as weight percent of samples ashed at 900 $^\circ\text{C}$.

of BaO: SrO is about 19:1, although Fig. 4 suggests that at higher barite concentrations the ratio is closer to 106:1. Thus barite is interpreted to contain an estimated 1–5% Sr substitution for Ba at different concentration levels.

The powders used for XRF were first ashed to 900 $^\circ\text{C}$ for loss on ignition (LOI) analysis; the wt% of LOI 600 $^\circ\text{C}$ (approximately equal to organic matter) and 900 $^\circ\text{C}$ (approximately equal to CO_2 lost from carbonate minerals) are also included in Supplemental Table 2. Thus the XRF samples had all organic matter and carbonate CO_2 removed prior to analysis. Because limited amorphous phases were observed in the samples, it is believed that the crystalline fraction of the bulk rock accounts for the vast majority of the elemental chemistry with calcite and dolomite decarbonated to oxides. Only elements interpreted to be present in mineral(s) identified by XRD are included in the data of Supplemental Table 2. Additional elements were analyzed, including TiO_2 (<0.8%), MnO (<0.06%), P_2O_5 (<0.2%), and a number of trace elements (sum $\leq 0.42\%$); however, the average concentration for these additional constituents was <1.0% per sample, and so they were simply excluded from the analysis and are not reported. The results of Supplemental Table 2 are normalized to 100% of the reported oxides, plus the lost CO_2 from carbonate minerals represented by LOI 900 $^\circ\text{C}$. On this basis, the elemental concentrations correspond very closely to the 100% basis for the crystalline fraction in XRD analysis.

4.3. XRD-XRF data integration

Quantitative mineralogy was estimated employing the inherently more accurate XRF elemental concentrations, allowing comparison to the semi-quantitative RIR estimates (Supplemental Tables 1 and 3). The abundance of each mineral phase identified was recalculated based on the XRF results, employing the stoichiometries of each corresponding PDF2 reference phase identified in each XRD sample (Table 1). For some mineral phases, elements in the XRF suite occur only in that phase; for example, among the phases identified, only albite contains Na, neglecting trace substitution of Na into cationic structural positions within other phases. Besides Na, other elements in this class include Ba + Sr (barite), and K (muscovite + illite). For all other

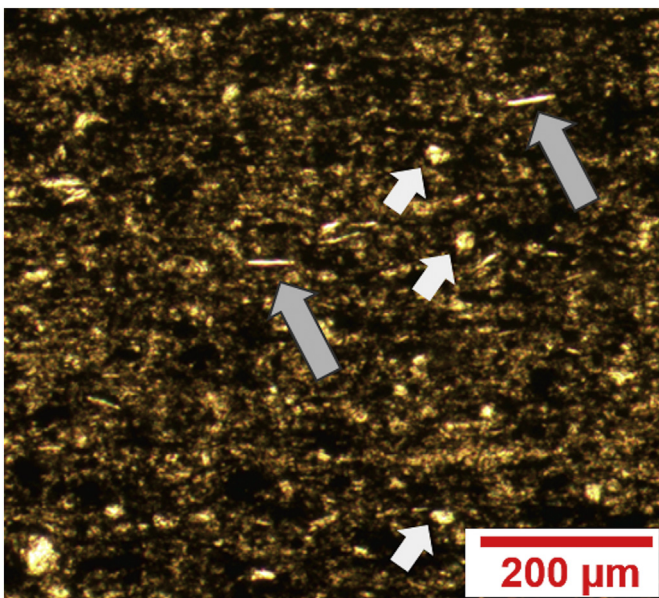


Fig. 3. Photomicrograph in plane-polarized light showing euhedral muscovite (large arrows) and detrital quartz grains (small arrows) within an illite-rich matrix.

minerals, elements present in abundance contribute to more than one phase, including Ca (calcite, dolomite), Mg (dolomite, chlorite), Fe (pyrite, chlorite), Al (all aluminosilicate phases), and Si (quartz and all aluminosilicate phases). To partition XRF concentrations across the mineral suite, a sequential procedure is needed, subject to the reality that both XRD and XRF concentrations sum to 100% of the crystalline (excluding organic) fraction. The serial approach developed first accounts for the single-phase elements, then the multiple-phase elements. Steps in this approach include:

1. All K is present either in muscovite or illite, and not easily discriminated by XRD, so “muscovite + illite” is quantified together using total K
2. All Na is present in albite, so total Na determines albite %
3. SrO + BaO concentrations are used to determine barite %.
4. MgO is partitioned between chlorite % and dolomite %, proportional to the ratios of the (001) and (104) peak heights, respectively, of these two phases. If no chlorite is observed by XRD, then all Mg is used for dolomite, and vice versa.
5. All residual FeO, after subtracting FeO from the Mg-determined chlorite %, is used to determine pyrite %.
6. All residual CaO, after subtracting that within dolomite %, is used to determine calcite %. If the resulting calcite CaO is negative, it is set as zero.
7. SiO₂ is partitioned between quartz, albite, chlorite, and muscovite + illite according to steps 1, 2 and 4 above, with quartz % determined from the residual after subtracting the sum of SiO₂ assigned to aluminosilicate phases.
8. The sum of crystalline components, excluding organic matter, is normalized to 100%.

Of the implicit assumptions in this procedure, the most significant are the lack of accounting for (a) isomorphous solid-state substitution for cations in the stoichiometry, and (b) adsorbed cations on clays. The procedure is largely an exercise in mass balance and mineral stoichiometry. In detail, for single phase elements (e.g. Na, K, and Ba + Sr), mineral concentrations for albite, muscovite + illite, and barite, respectively, were calculated as follows:

$$X_{\min} = X_{\text{ox}} [G_{\min}/(n \cdot G_{\text{ox}})] \tag{1}$$

where: X_{\min} = weight percent of mineral phase; X_{ox} = weight percent of the XRF-determined elemental oxide; G_{\min} = gram formula weight of the mineral phase; G_{ox} = gram formula weight of the elemental oxide; and n = ratio of moles of element in mineral phase to moles in the oxide.

For example, XRF K₂O (2 mol K) applied to XRD muscovite/illite (reference stoichiometry KAl₂(AlSi₃)O₁₀(OH)₂) yields $n = 0.5$. These equations are applied in steps 1–3 above to determine muscovite + illite, albite, and strontian barite concentrations.

In step 4, for samples with detectable concentrations of both chlorite and dolomite, MgO is partitioned between these two phases (1 = chlorite, 2 = dolomite) according to R_{12} , the ratio of baseline-corrected peak-height counts per second (cps) for chlorite to dolomite:

$$X_{\text{chl}} = X_{\text{MgO}} \cdot [R_{12}/(R_{12} + 1)] \cdot [G_{\text{chl}}/(2.5G_{\text{MgO}})] \tag{2}$$

$$X_{\text{dol}} = X_{\text{MgO}} \cdot [1/(R_{12} + 1)] \cdot [G_{\text{dol}}/G_{\text{MgO}}] \tag{3}$$

In addition to having a partition with Mg, chlorite and dolomite also partition Fe and Ca with pyrite and calcite, respectively. For these two

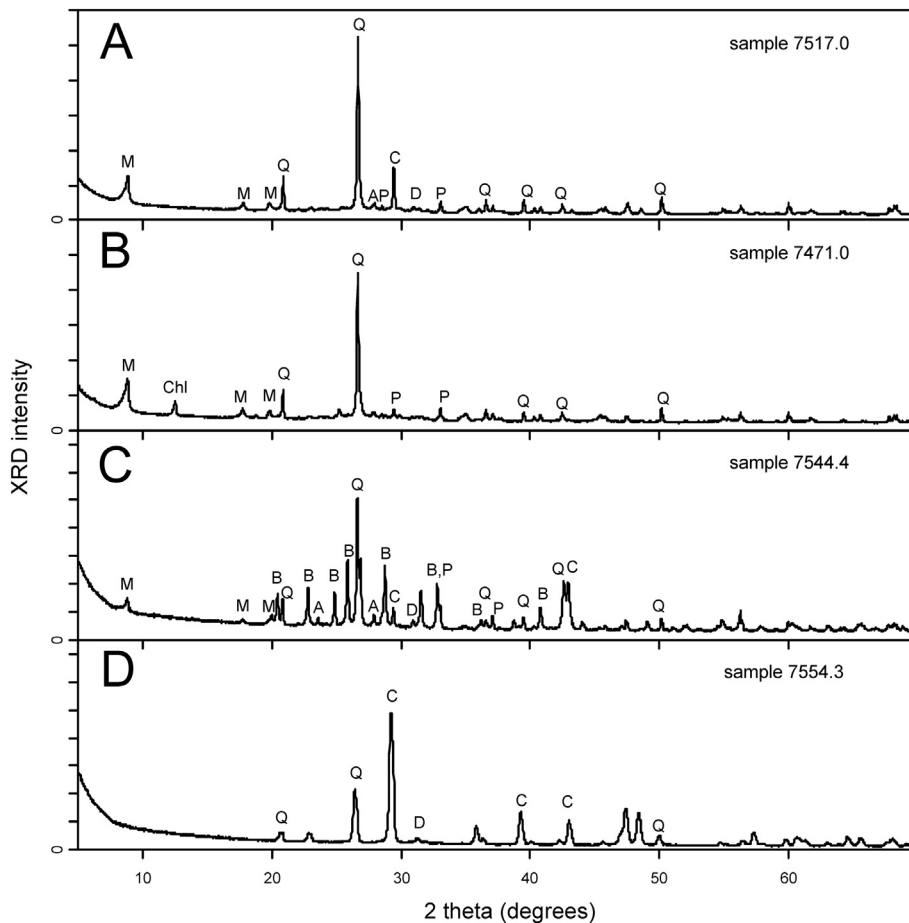


Fig. 5. X-ray diffraction traces of typical sample of (A) non-calcareous shale, (B) calcareous shale, (C) carbonate-rich shale, and (D) silty limestone. Legend: M = muscovite + illite; Chl = chlorite; Q = quartz; B = barite; P = pyrite; C = calcite; D = dolomite; A = albite. Sample IDs indicated at upper right of plots.

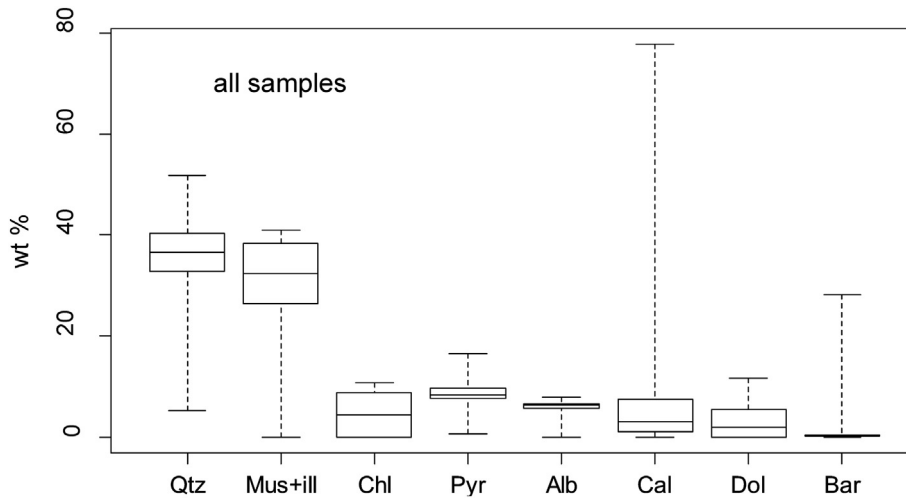


Fig. 6. Boxplot of XRD-XRF mineralogy for all samples, as percent of crystalline fraction. Median is the black horizontal bar; box is the central 50% of sample frequency. Whisker ends are minima and maxima.

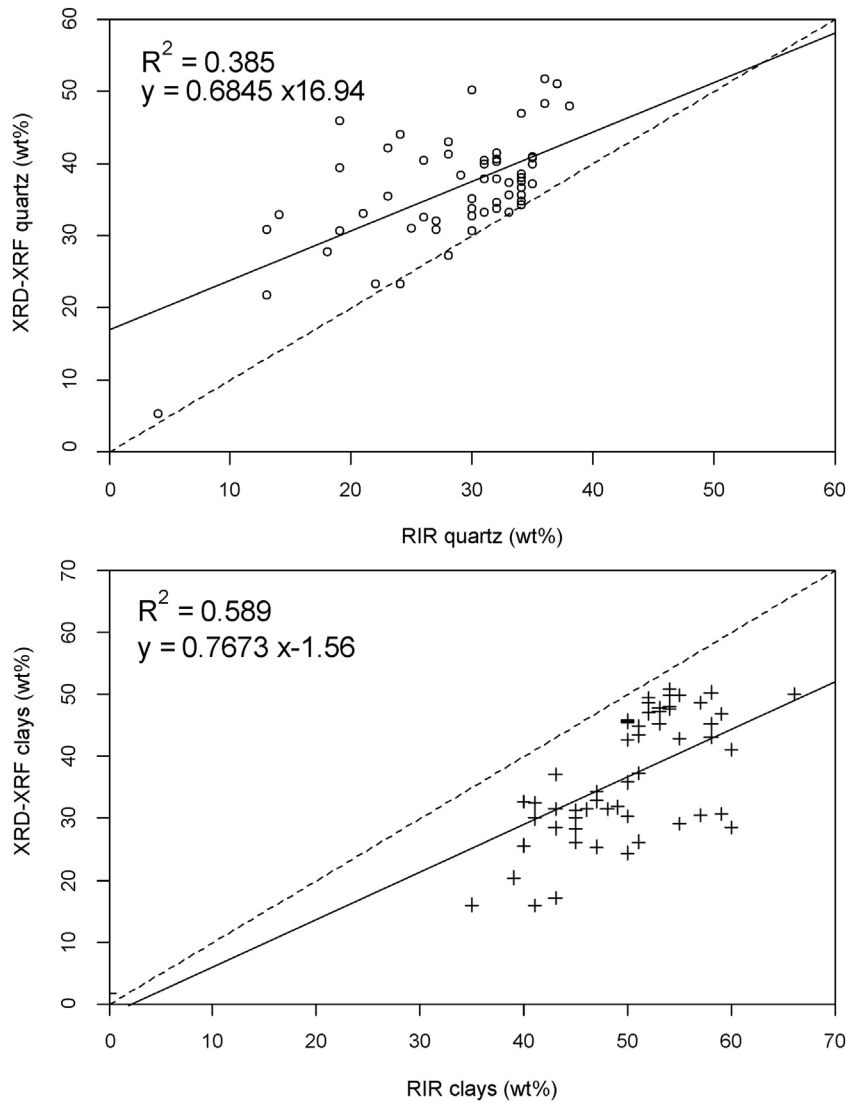


Fig. 7. Comparison of quartz (top) and clay mineral sum (bottom) between RIR and XRD-XRF interpretations, in percent of crystalline fraction.

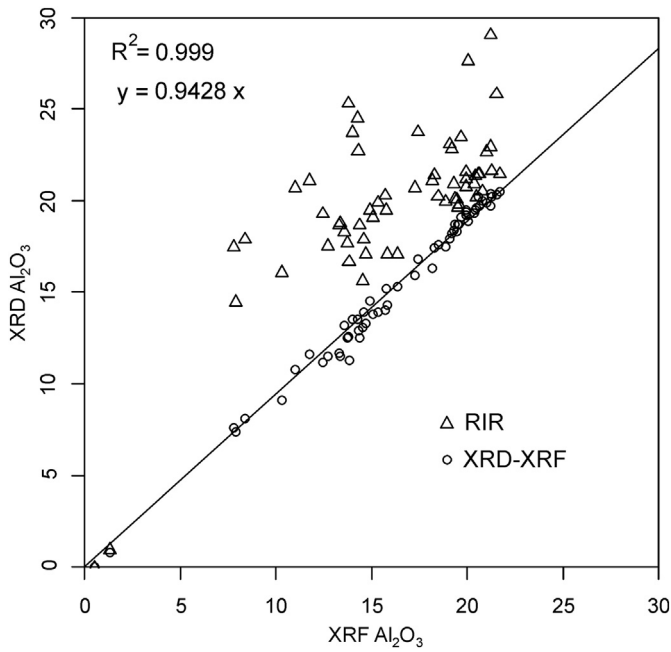


Fig. 8. Comparison of Al₂O₃ from XRF and calculated Al₂O₃ from XRD/XRF mineralogy (circles) and RIR XRD mineralogy (triangles). Regression line represents relationship between XRF Al₂O₃ and calculated XRD/XRF Al₂O₃.

elements, the concentrations as an elemental oxide partitioned into minerals in Eqs. (2) and (3) may be subtracted from the total XRF FeO and CaO, respectively:

$$X_{\text{pyr}} = [X_{\text{FeO}} - X_{\text{chl}} * (G_{\text{FeO}}/G_{\text{chl}})] * (G_{\text{chl}}/G_{\text{FeO}}) \quad (4)$$

$$X_{\text{cal}} = [X_{\text{CaO}} - X_{\text{dol}} * (G_{\text{CaO}}/G_{\text{dol}})] * (G_{\text{cal}}/G_{\text{CaO}}) \quad (5)$$

where the X notation describes mineral concentrations or wt% oxide and the G values are formula weights of either minerals or XRF oxides.

Once steps 1 to 6 were complete, in step 7 residual SiO₂ was used to estimate silica in quartz using all SiO₂ not partitioned into silicate phases, according to stoichiometries:

$$X_{\text{qtz}} = X_{\text{SiO}_2} - G_{\text{SiO}_2} [2.2X_{\text{chl}}/G_{\text{chl}} + 3X_{\text{mus}}/G_{\text{mus}} + 3X_{\text{alb}}/G_{\text{alb}}] \quad (6)$$

Then the absolute abundance of each mineral phase (X_m) as a portion of the inorganic fraction is calculated by normalizing the mineral abundances to 100%.

Similarly, using the normalized XRD-XRF quantification, Al₂O₃ may be calculated from the silicate mineral concentrations:

$$X_{\text{Al}_2\text{O}_3} = G_{\text{Al}_2\text{O}_3} [1.65X_{\text{chl}}/G_{\text{chl}} + 1.5X_{\text{mus}}/G_{\text{mus}} + 0.5X_{\text{alb}}/G_{\text{alb}}] \quad (7)$$

The results of this procedure are presented in Supplemental Table 3 and are based on both the XRD results (identity of minerals found, peak-height ratio of chlorite to dolomite if both are present) and

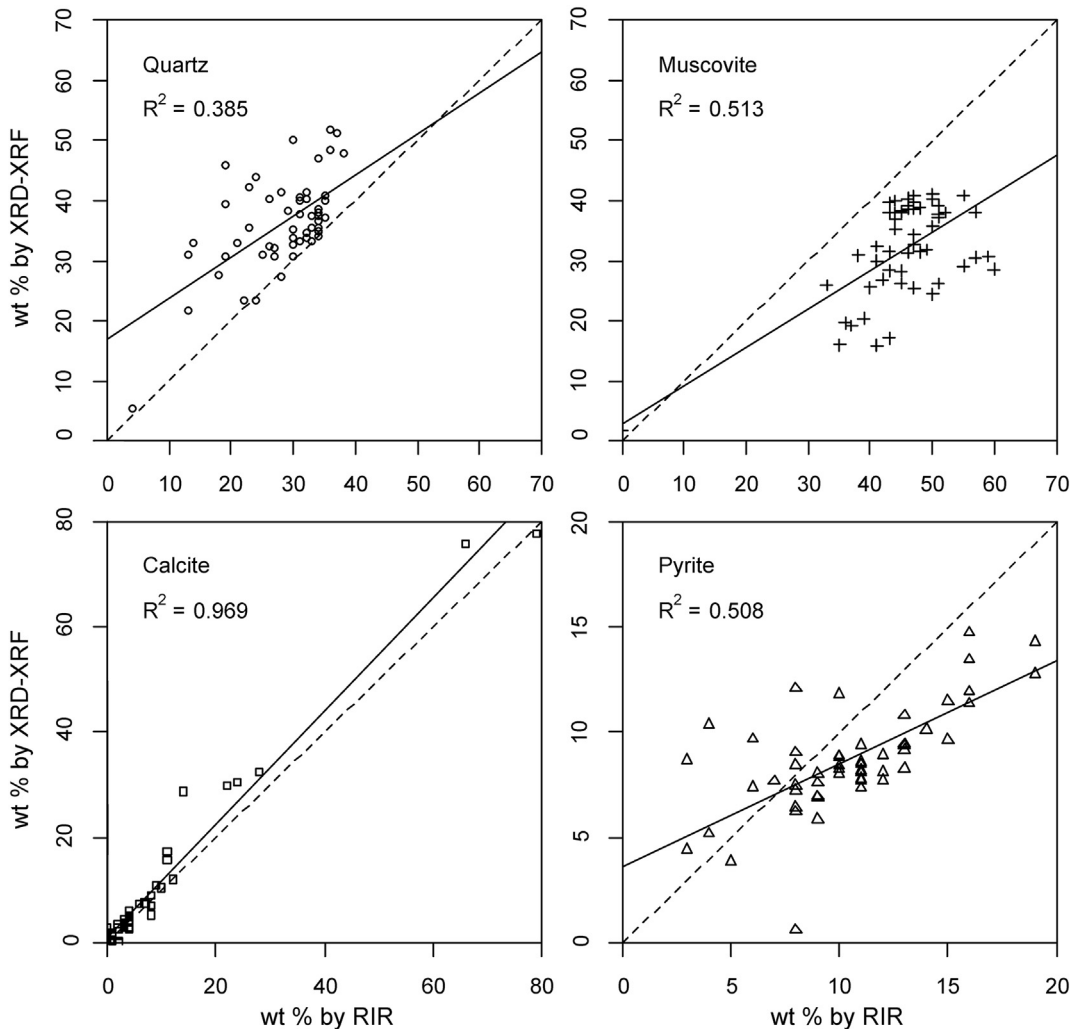


Fig. 9. Comparison of (in clockwise direction) quartz, muscovite + illite, calcite, and pyrite between RIR and XRD-XRF interpretations, in percent of crystalline fraction.

XRF elemental concentrations. These results will be referred to as XRD-XRF mineralogy.

Implementing the partitioning procedure encountered minor difficulties in the Marcellus Shale samples. In two samples (7505.0 and 7538.0), calcite concentration calculated by XRD-XRF was slightly negative but within 1% of zero. These were both samples in which only minor concentrations of calcite had been detected by XRD. These XRD-XRF calcite values were set to zero. In all samples with no XRD detectable peaks for chlorite or dolomite, both were set to zero and the XRF MgO was not employed, despite minor (<1.0%) MgO being present by XRF. Similarly, zero values for XRD-XRF concentration of both dolomite and calcite were honored in three such cases (7485.6, 7523.0, 7554.4) and XRF CaO was not employed. Any resulting mass-balance error was removed by normalization. The cause for these anomalous results is ascribed to (1) the potential for minor concentrations of Mg, Na, and Ca as adsorbed cations on clays or as trace substitutions for other cations in minerals, or (2) difficulty in detecting and quantifying calcite or, especially, dolomite by XRD at low levels.

Fig. 5 shows a plot of XRD traces of four type lithologies occurring within the core. From top to bottom, these are a calcareous shale; a non-calcareous shale; a highly calcareous shale; and a muddy limestone. Most peaks used for identification lie in the 7–50 degree 2-theta region. The top 2 lithologies are relatively common in the core, while the bottom 2 show more unusual high-barite and high-calcite suites. Minerals that are generally abundant where present include quartz, illite/muscovite, and chlorite. Calcite and dolomite may be present or absent and, except

in unusual limey samples such as 7554.3 ft., in low concentration. Pyrite and albite are present throughout, but in minor concentrations. Barite is generally absent but, where found, is often rather abundant and shows multiple peaks on the diffractogram, as in 7544.4 ft. (Fig. 5). These samples emphasize the greater ease in detecting more abundant phases (quartz, clays) than those with minor peaks, especially albite, pyrite, and dolomite.

Fig. 6 shows a boxplot of XRD-XRF mineralogy results for all samples, showing median (thick horizontal band), the middle 2 quartiles of frequency (box) and minima/maxima (“whiskers”). Quartz and muscovite + illite are the dominant minerals in most samples, although their low minima suggest a few low values. The rest of the minerals are less abundant, although calcite and dolomite appear to have a few very high outliers and are likely non-normally distributed. Chlorite, pyrite, albite, and dolomite all have medians in the 1–10 wt% range and no extreme outliers. Thus, the mineralogy has three dominant phases and the rest minor, although calcite and barite appear to be very high in some samples.

4.4. Comparison of XRD-XRF to RIR results

Fig. 7 compares XRD-XRF to RIR results for quartz (top) and summed clay minerals muscovite/illite plus chlorite (bottom). Together, these minerals constitute an average of 72.9% and 78.0% of the crystalline fraction in the XRD-XRF and RIR datasets, respectively. That is, these minerals represent the majority of crystalline matter present, with

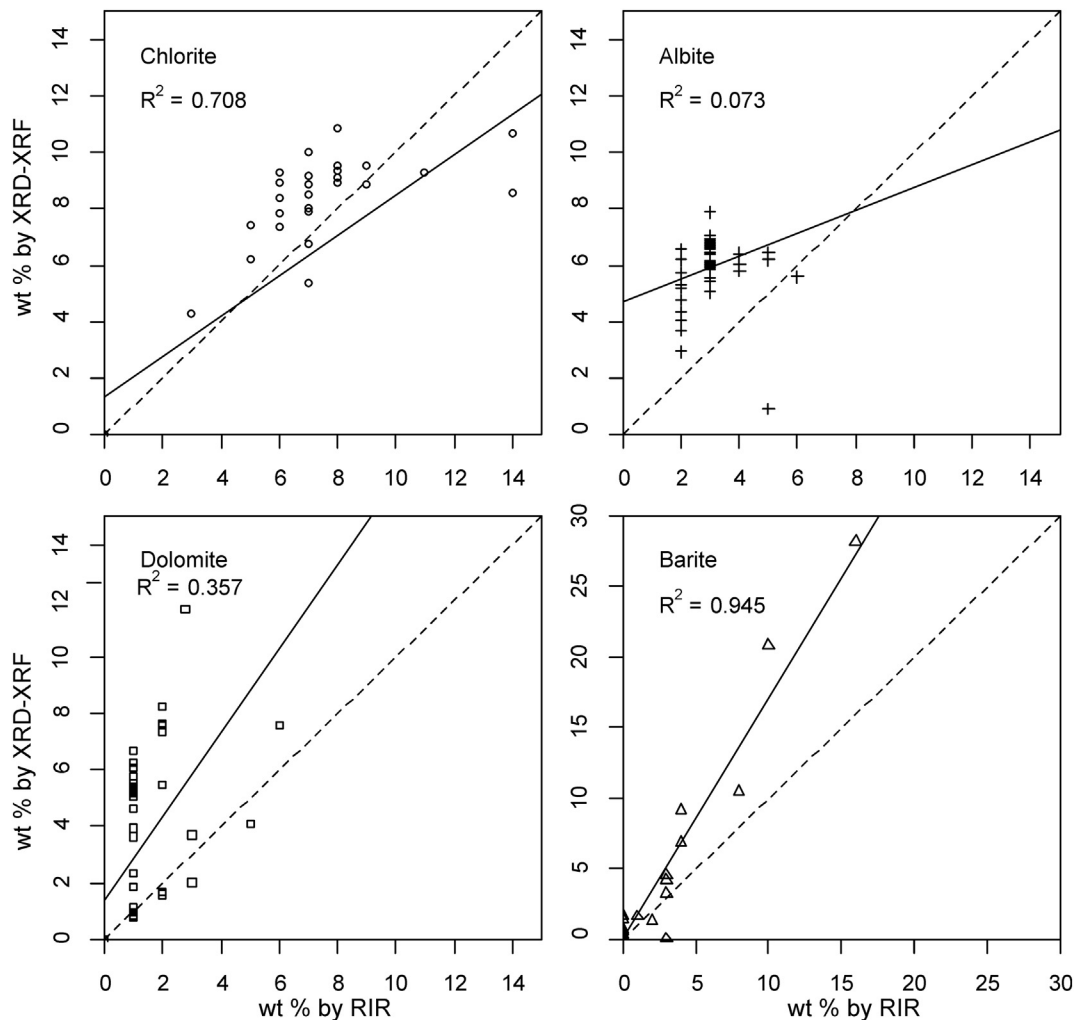


Fig. 10. Comparison of (in clockwise direction) chlorite, albite, dolomite, and barite between RIR and XRD-XRF interpretations, in percent of crystalline fraction.

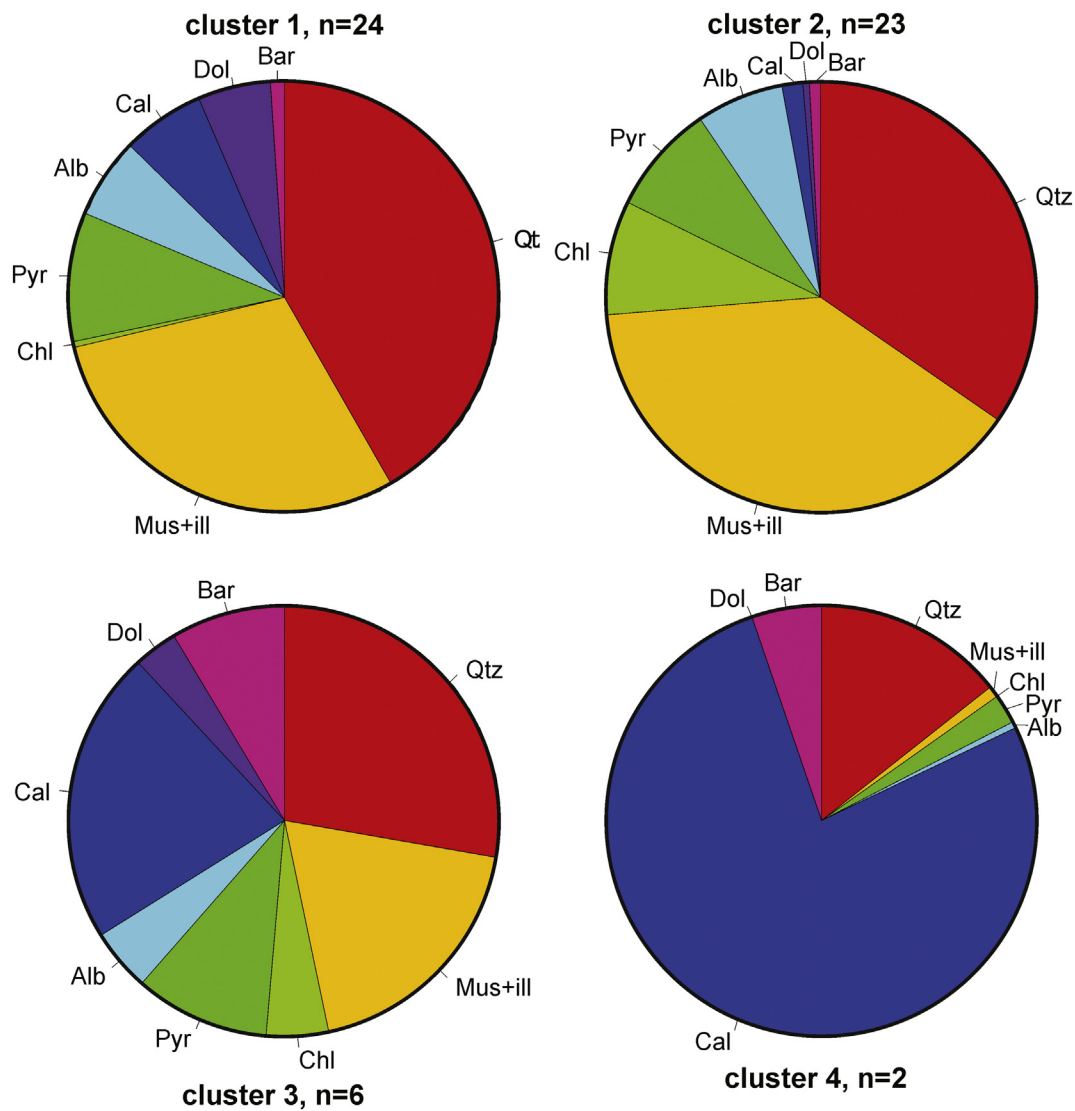


Fig. 12. Circle charts of mineral concentration (%) for cluster centroids, in percent of crystalline fraction.

while calcite and dolomite are present in similar concentrations. In cluster 2, calcite and dolomite are nearly absent and chlorite accounts for about 9%. The cluster 1 samples are concentrated in the lower Marcellus Shale (7503.0–7556.0 ft) while the cluster 2 samples are at the top (7455.0–7500.0 ft). There is little stratigraphic overlap. The upper Marcellus Shale samples are therefore chloritic shale, while the

lower samples contain calcareous shale. When chlorite is present, dolomite is largely absent, and vice versa.

Clusters 3 and 4 are both small groups that seem anomalous. Cluster 3 is a quartz-muscovite shale with higher concentrations of the other mineral phases, in particular calcite and/or barite. Cluster 4 comprises only 2 samples and is 75% calcite with minor quartz and barite. Thus cluster 3 is a highly-calcareous shale and cluster 4 a muddy limestone. Petrographic analysis of these clusters shows that samples within cluster 4 exhibit an abundance of fossils, primarily styliolinids and thin-walled mollusc shells, within a matrix composed of clay and displacive calcite (Fig. 13). Fossils display both drusy and blocky cements within the larger intragranular pores. A dolomite vein also runs through one of the two samples. These two observations help to account for the abundant carbonate content. Photomicrographs of cluster 3 samples are dominated by an illite-muscovite matrix with sparse fossil-rich lamina or carbonate-replaced radiolaria. Differences in matrix composition, biogenic sediments, and diagenetic phases likely account for the separate clustering among these samples.

Fig. 14 shows barplots of mineral distributions in various clusters. Quartz and muscovite are highest in clusters 1 and 2, lower in cluster 3, and very low in the limestone cluster. Calcite and barite are both present in the anomalous clusters 3 and 4. Pyrite and albite tend to be

Table 3
Percent mean and standard deviation of mineral phases for each cluster.

Mineral phase	Cluster 1 (n = 24)		Cluster 2 (n = 23)		Cluster 3 (n = 6)		Cluster 4 (n = 2)	
	Avg. (%)	± (%)	Avg. (%)	± (%)	Avg. (%)	± (%)	Avg. (%)	± (%)
Qtz	41.62	5.60	34.67	2.43	27.69	4.92	14.24	12.68
Musc + ill	29.54	3.80	38.94	1.42	18.96	3.76	0.82	1.16
Chl	0.44	1.51	8.64	1.01	4.71	5.36	0.00	0.00
Pyr	9.57	2.63	8.24	1.39	10.10	3.54	2.20	2.27
Alb	6.03	0.73	6.56	0.27	4.63	1.33	0.45	0.63
Cal	5.88	4.94	1.60	1.25	22.00	12.98	74.73	0.84
Dol	5.93	2.00	0.53	0.93	3.33	1.19	2.36	0.52
Bar	1.00	2.08	0.82	1.45	8.58	12.64	5.20	7.26

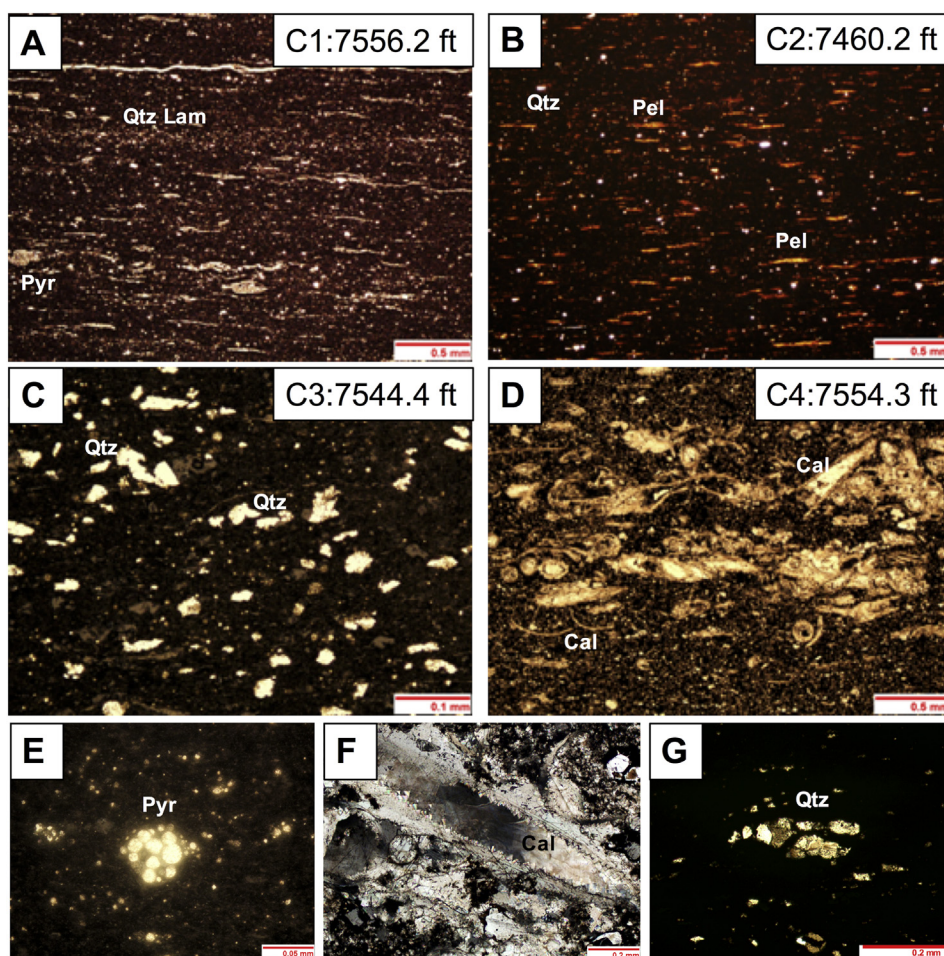


Fig. 13. Photomicrograph examples from each mineralogical cluster. A: Reflected light image of cluster 1 displaying quartz-rich laminations (Qtz Lam) and visible pyrite framboids (Pyr). B: Photomicrograph of a cluster 2 sample in plane polarized light showing quartz silt (Qtz) and clay-rich peloids (Pel). C: Plane polarized light image of cluster 3 showing abundant quartz silt. D: Cluster 4 example in plane polarized light showing abundant styliolinid and thin-walled mollusc shells composed of calcite (Cal) within a clay-calcite matrix. E: Visible pyrite framboid in reflected light. F: Styliolinid displaying multiple generations of calcite cement. G: Closer view into the abundant quartz silt. F and G photomicrographs were taken under cross-polarized light.

similar in concentration in clusters 1–3 and lowest in the limestone. Chlorite and dolomite show inverse abundance in cluster 1 and 2 shales and are absent in cluster 4.

5. Discussion

5.1. Comparisons of RIR- and XRD-XRF-derived mineralogy

Comparison of the RIR to XRD-XRF mineralogy results clearly indicates that for all phases except calcite and barite, the two quantitative data sets are in only general agreement, with significant differences between the two. Correlations are poorest for the minerals dolomite and albite, both of which occur at RIR concentrations below 6% and in many cases $\leq 3\%$, which is arguably the lower detection limit of RIR methodology.

It is clear, as well, that the RIR method overestimates clay minerals and underestimates quartz in comparison to XRD-XRF. We interpret this to likely be the result of exaggeration of XRD peak heights for clay minerals and mica due to preferred sample orientation. This is supported by the observation that SiO_2 from XRF and from XRD-XRF mineralogy are (de facto) consistent, but in addition Al_2O_3 is highly consistent between the two datasets, by mass balance, despite the fact that alumina from the XRF dataset were not employed in the XRD-XRF procedure. These observations support the interpretation

that the XRD-XRF values are inherently more accurate than the RIR interpretations. They are also less arbitrary, as the uncalibrated RIR results are based on a somewhat arbitrary selection of reference samples and RIR parameters.

5.2. Applications and limitations of cross-quantification methodology

There are some issues with the XRD-XRF results in this dataset for minerals present at low concentrations, especially albite, dolomite, and calcite. Besides simple higher relative error at low concentrations, these issues are possibly related to concentrations of adsorbed cations on clays not being measured and considered, and while this adsorbed cation fraction is unlikely to have been large, neglecting it could have an effect on low-concentration minerals in the calculation method. The simplest solution to this problem would be to displace adsorbed cations with a cation not measured by XRF, such as ammonium, prior to XRF analysis. This could ensure that the elemental analysis is performed on a fraction containing only crystalline inorganic compounds.

A second issue involves evaluation of amorphous phases. For purposes of our calculations, we made the assumption that our XRF data represented only the crystalline fraction of each sample. However, during petrographic analysis, some radiolarians were observed in organic-rich intervals, suggesting that some amorphous biogenic silica could

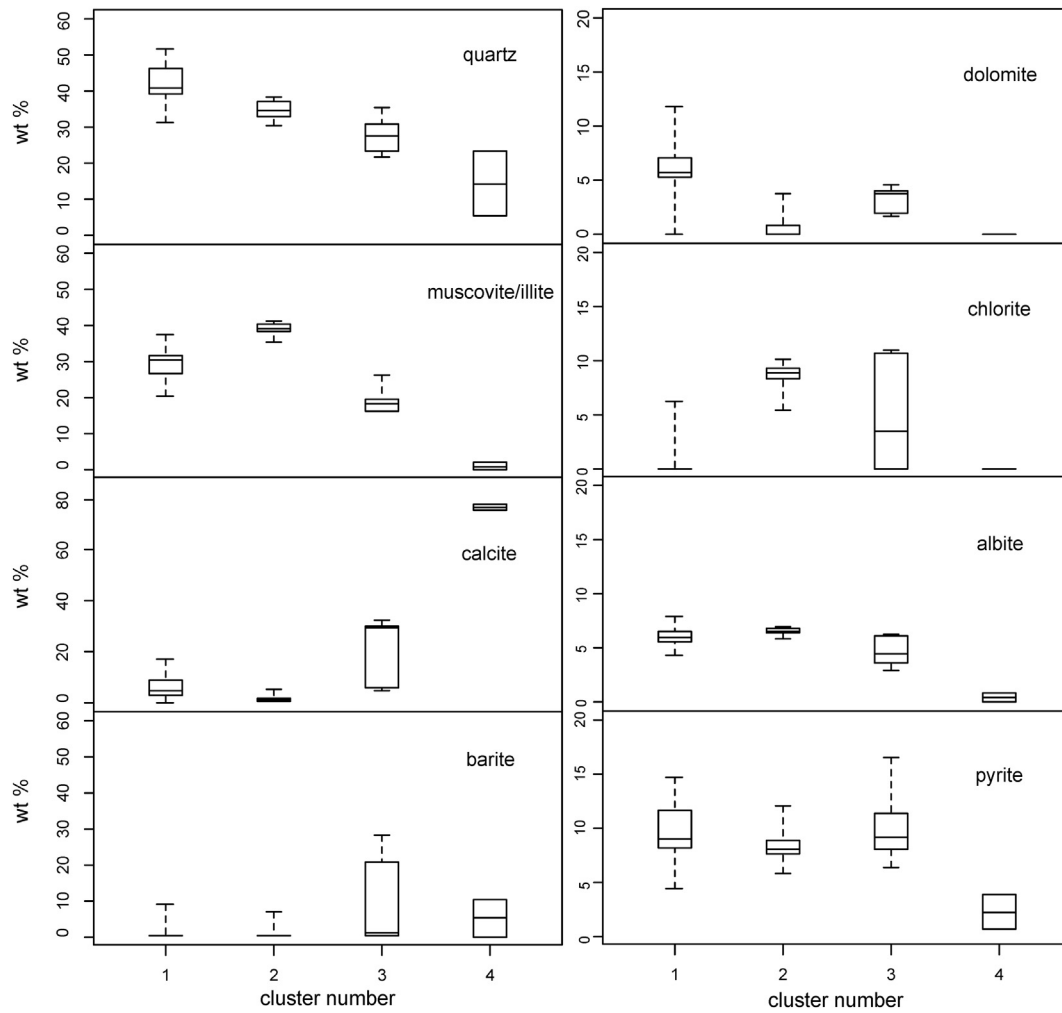


Fig. 14. Boxplots of mineral concentration for cluster centroids, in percent of crystalline fraction.

be present if the tests have not undergone recrystallization (Fig. 15). Amorphous iron-oxide phases are deemed unlikely. Scanning electron microscopy and thin section petrography both confirm abundant crystalline pyrite, present both as framboids and euhedral crystals (Fig. 15). In a sedimentary environment where pyrite is geochemically stable, oxidation products are unlikely. Furthermore, the mass-balance check of Fig. 8 using Al_2O_3 is strong evidence that the integrated XRD-XRF results are accurate and that no phases were omitted from the analysis.

The XRD-XRF method in this investigation was based upon a set of rules that appears to have been successful for this particular mineral suite, presenting a potential quantitative approach for establishing mineralogy in marine shales. The XRD-XRF workflow incorporates datasets that are often required for further interpretation of mudrocks and presents a methodology for determining bulk mineralogy within rocks of multiple unknown phases. However, the presence of multiple minerals containing a single element is a complication that needs to be worked out for dataset-specific conditions, on a case by case basis.

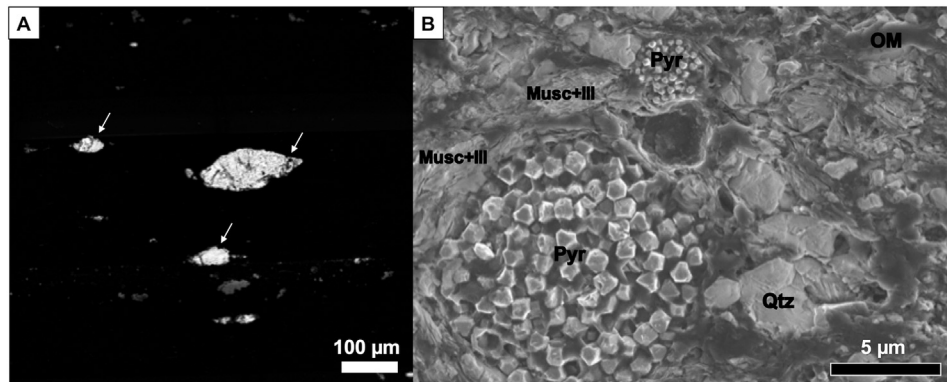


Fig. 15. A: Photomicrograph of fossilized radiolarians (arrows) taken in plane-polarized light. B: SEM image of micron-scale features showing the presence of pyrite framboids. Both images are from the same sample, depth 7544.9 ft., within the organic-rich interval of the Marcellus Shale. Legend: quartz (Qtz), pyrite (Pyr), illite + muscovite (Musc + Ill), organic matter (OM).

5.3. Marcellus Shale mineralogy

Quartz, illite + muscovite, and albite covary and are inversely correlated with calcite and dolomite; that is, there are distinct siliciclastic and calcareous shale zones that occur in the top and bottom, respectively, of the Marcellus Shale unit (Supplemental Table 3). Key indicator minerals of this difference in mineralogy are chlorite, dolomite, and calcite. Of minerals containing Mg, chlorite dominates the upper siliciclastic zone, whereas dolomite dominates the calcareous zone, with a thin interval in the middle (7488.0–7500.6 ft.; 2282.3–2286.2 m) in which both minerals occur (Fig. 16). The transition from dolomite to chlorite could reflect changes in sediment provenance and perhaps influx from a metasedimentary source. Chlorite could also have been produced by hydrothermal alteration of muscovite, influenced by Mg-rich brines that have been reported within the Marcellus Shale (Haluszczak et al., 2013). However, it seems unlikely that such brine alteration or metamorphism would only produce chlorite in the upper part of the Marcellus Shale and not affect muscovite within the lower section. The consistent occurrence of chlorite within the upper Marcellus Shale suggests that chlorite may be a primary extrabasinal mineral phase.

The transition from cluster 1 mineralogy in the lower Marcellus Shale to cluster 2 in the chloritic upper zone possibly reflects changes in sedimentation patterns from pelagic-dominated to hemipelagic-dominated sedimentation. Clusters 1, 3, and 4 in the calcareous lower Marcellus Shale may, correspondingly, reflect an intrabasinal provenance. Comparison of stratigraphic cluster distribution to TOC content indicates lower TOC values are correlative to the onset of cluster 2 mineralogical deposition (Fig. 16). These observations suggest that the mineralogy of the Marcellus Shale may be indicating primary depositional influences on organic carbon preservation.

5.4. Errors and uncertainty in XRD-XRF results

While the XRD-XRF approach resolves some well-known difficulties in XRD interpretation, there are still potential sources of error in implementation:

1. The method depends on accurate and complete identification of all crystalline phases present, as does the RIR and other methods.
2. XRF analysis may include concentrations of elements that are not within the crystalline fraction, but in amorphous phases, organic matter, or adsorption sites on clays. Care must be taken to identify, pre-treat, or correct for such concentrations, so that the basis for both XRD and XRF analyses are close to identical. This is especially the case for elements in low abundance, as Ca, Mg, and Na were in some of the Marcellus Shale samples.
3. The stoichiometry of the identified minerals must match that of the phase in the sample itself. In this investigation, the idealized reference PDF formulae were employed. This is subject to error, particularly with respect to deviations from ideal caused by trace substitution. A better approach may be to individually characterize crystal chemistries using SEM or microprobe methods.

In XRD interpretation, the relative error tends to be greatest for phases in minor concentration. This is likely to remain true for application of XRD-XRF integration.

6. Conclusions

Traditional XRD methodologies commonly produce semi-quantitative results and are subject to error in quantifying minerals

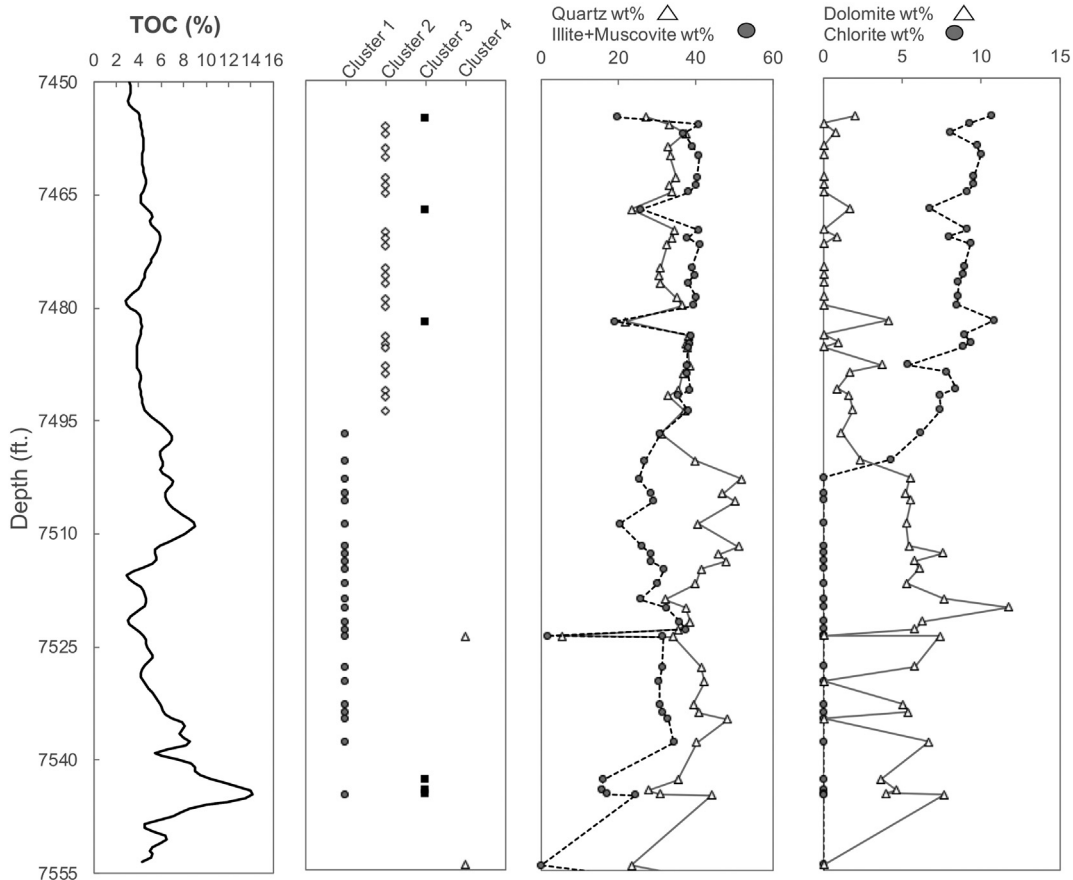


Fig. 16. Mineralogical cluster, quartz, illite + muscovite, chlorite, and dolomite stratigraphic distribution paired with uranium-predicted total organic carbon (TOC) log from the sampled well (Paronish, 2018).

that show preferred orientations (e.g. clay minerals and mica). Here we produce a workflow for quantitatively determining mineralogy via integration of XRD and XRF data sets using marine shale from the Marcellus Shale. Key findings include:

- Nine mineral phases were identified in some or all samples including quartz, muscovite, illite, pyrite, chlorite, albite, calcite, dolomite, and barite.
- XRD-XRF integration allowed determination of quantitative mineral abundances for all 55 samples, correcting for overestimation of clays and mica (i.e. illite + muscovite) produced using XRD results alone.
- Cluster analysis of XRD-XRF mineralogy identified four mineralogical facies within the Marcellus Shale that may reflect potential depositional influences on differences in organic matter content between the upper and lower Marcellus.

The technique may be broadly applicable to the determination of mineralogy in shale and other mudrocks, although it is likely to require modification of the specific sequential algorithm employed to handle different mineral assemblages on a case-by-case basis. Further refinements to the approach could involve several directions, including establishing protocols for adsorbed cation removal and use of SEM-EDS to empirically quantify stoichiometries. However, it seems likely that techniques of this type, based on quantitative elemental data in combination with semi-quantitative XRD results, could mitigate the long-known preferred-orientation effects on accuracy of XRD-based quantitative mineralogy and prove useful to academic and industrial communities alike.

Acknowledgements

This research was funded by the USDOE National Energy Technology Laboratory as part of the Marcellus Shale Energy and Environmental Laboratory project (MSEEL; Award DE-FE0024297). The junior author was also funded on NSF EPSCOR Track 2 RII, project ETD-37 (Award OIA-1632892). We acknowledge Northeast Natural Energy LLC for providing access to the core material. Contractual elemental chemistry was performed using x-ray fluorescence and loss-on-ignition by Rick Conrey and Lauren Wagoner of the Hamilton Analytical Laboratory, Taylor Science Center, Hamilton College.

Appendix A. Supplementary material

Supplementary data to this article can be found online at <https://doi.org/10.1016/j.sedgeo.2018.04.007>.

References

- Blanchard, P.E.R., Grosvenor, A.P., Rowson, J., Hughes, K., Brown, C., 2016. Identifying calcium-containing mineral species in the HEB tailings management facility at McClean Lake, Saskatchewan. *Applied Geochemistry* 73, 98–108.
- Braun, G.E., 1986. Quantitative analysis of mineral mixtures using linear programming. *Clays and Clay Minerals* 34, 330–337.
- Burkett, D.A., Graham, I.T., Ward, C.R., 2015. The application of portable x-ray diffraction to quantitative mineralogical analysis of hydrothermal systems. *Canadian Mineralogist* 53, 429–454.
- Chung, F.H., 1975a. Quantitative interpretation of x-ray diffraction patterns of mixtures. I. Matrix-flushing method for quantitative multicomponent analysis. *Journal of Applied Crystallography* 7, 519–525.
- Chung, F.H., 1975b. Quantitative interpretation of x-ray diffraction patterns of mixtures. III. Simultaneous determination of a set of reference intensities. *Journal of Applied Crystallography* 8, 17–19.
- Dennison, J.M., Hasson, K.O., 1976. Stratigraphic cross-section of Hamilton Group (Devonian) and adjacent strata along south border of Pennsylvania. *The American Association of Petroleum Geologists Bulletin* 60, 278–298.
- Dennison, J.M., Textoris, D.A., 1988. Devonian Tioga ash beds. *West Virginia Geological and Economic Survey. Circular C-42*, 15–16.
- Ellwood, B.B., Algeo, T.J., Hassani, A.E., Tomkin, J.H., Rowe, H.D., 2011. Defining the timing and duration of the Kacac interval within the Eifelian/Givetian boundary GSSP, Mech Iradence, Morocco, using geochemical and magnetic susceptibility patterns. *Palaeogeography, Palaeoclimatology, Palaeoecology* 304, 74–84.
- Enomoto, C.B., Olea, R.A., Coleman Jr., J.L., 2014. Characterization of the Marcellus Shale based on computer-assisted correlations of wireline logs in Virginia and West Virginia. *US Geological Survey-Scientific Investigations Report* (21 pp).
- Ettensohn, F.R., 1985. The Catskill Delta complex and the Acadian Orogeny: a model. In: Woodrow, D.L., Sevon, W.D. (Eds.), *The Catskill Delta*. Geological Society of America Special Paper No. 201, pp. 39–50.
- Ettensohn, F.R., Lierman, T.R., 2013. Large scale tectonic controls on the origin of Paleozoic dark shale source rock basins; examples from the Appalachian foreland basin, Eastern United States. *American Association of Petroleum Geologists. Memoir* 100, 95–124.
- Ferrier, K.L., Kirchner, J.W., Riebe, C.S., Finkel, R.C., 2010. Mineral-specific chemical weathering rates over millennial timescales: measurements at Rio Icaos, Puerto Rico. *Chemical Geology* 277, 101–114.
- Grattin-Bellew, P.E., 1975. Effects of preferred orientation on X-ray diffraction patterns of gypsum. *American Mineralogist* 60, 1127–1129.
- Haluszczak, L.O., Rose, A.W., Kump, L.R., 2013. Geochemical evaluation of flowback brine from Marcellus gas wells in Pennsylvania, USA. *Applied Geochemistry* 28, 55–61.
- Hausen, D.M., Odekirk, J.R., 1991. XRD mineralogical logging of drill samples from gold and copper mining operations. *Ore Geology Reviews* 6, 107–118.
- He, C., Li, M., Liu, W., Barbot, E., Vidic, R.D., 2014. Kinetics and equilibrium of barium and strontium sulfate formation in Marcellus Shale flowback water. *Journal of Environmental Engineering* 2, B4014001. [https://doi.org/10.1061/\(ASCE\)EE.1943-7870.0000807](https://doi.org/10.1061/(ASCE)EE.1943-7870.0000807).
- Hibbard, J.P., van Staal, C.R., Rankin, D.W., 2010. Comparative analysis of the geological evolution of the northern and southern Appalachian orogeny Late Ordovician-Permian. In: Tollo, R.P. (Ed.), *From Rodinia to Pangea: The Lithotectonic Record of the Appalachian Region*. Geological Society of America Memoir 206, pp. 51–69.
- Hillier, S., 2000. Accurate quantitative analysis of clay and other minerals in sandstones by XRD: comparison of a Rietveld and a reference intensity ratio (RIR) method and the importance of sample preparation. *Clay Minerals* 35, 291–302.
- Hupp, B.N., 2017. Provenance of the Hamilton Group: A Study of Source-to-Sink Relationships within the Middle Devonian Central Appalachian Basin. (M.S. Thesis). West Virginia University, Morgantown, West Virginia, USA (128 pp.).
- International Center for Diffraction Data (ICDD), 2004. PDF-2 diffraction database. <http://www.icdd.com/products/pdf2.htm>.
- Jenkins, R., 1989. Experimental procedures. In: Bish, D.J., Post, J.E. (Eds.), *Modern Powder Diffraction: Reviews in Mineralogy* 20. Mineralogical Society of America, Washington, D.C., pp. 47–71.
- Kelsey, C.H., 1965. Calculation of the C.I.P.W. norm. *Mineralogical Magazine* 34, 276–282.
- Klug, H.P., Alexander, L.E., 1974. *X-Ray Diffraction Procedures: For Polycrystalline and Amorphous Materials*. 2nd edition. John Wiley & Sons, New York (992 pp.).
- Kolka, R.K., Laird, D.A., Nater, E.A., 1994. Comparison of four elemental mass balance methods for clay mineral quantification. *Clays and Clay Minerals* 42, 437–443.
- Lash, G.G., Engelder, T., 2011. Thickness trends and sequence stratigraphy of the Middle Devonian Marcellus Formation, Appalachian Basin: implications for Acadian foreland basin evolution. *American Association of Petroleum Geologists Bulletin* 95, 61–103.
- Loubser, M., Verryn, S., 2008. Combining XRF and XRD analyses and sample preparation to solve mineralogical problems. *South African Journal of Geology* 111, 229–238.
- Medrano, M.D., Piper, D.Z., 1991. A normative-calculation procedure used to determine mineral abundances in rocks from the Montpelier Canyon Section of the Phosphoria Formation, Idaho: a tool in deciphering the minor-element geochemistry of sedimentary rocks. *US Geological Survey Bulletin* 2023A (23 pp.).
- Milici, R.C., Swezey, C.S., 2014. Assessment of Appalachian basin oil and gas resources; Devonian gas shales of the Devonian Shale-Middle and Upper Paleozoic total petroleum system. *U.S. Geological Survey Professional Paper* 1708 (81 pp.).
- Murtagh, F., Legendre, P., 2014. Ward's hierarchical agglomerative clustering method: which algorithms implement Ward's criterion? *Journal of Classification* 31, 274–295.
- Paronish, T., 2018. Meso- and Macro-scale Facies and Chemostratigraphic Analysis of Middle Devonian Marcellus Shale in Northern West Virginia, USA. (M.S. Thesis). West Virginia University, Morgantown, West Virginia, USA (382 pp.).
- Parrish, C.B., 2013. Insights Into the Appalachian Basin Middle Devonian Depositional System from U-Pb Zircon Geochronology of Volcanic Ashes in the Marcellus Shale and Onondaga Limestone. (M.S. Thesis). West Virginia University, Morgantown, West Virginia, USA (149 pp.).
- Piga, G., Santos-Cubedo, A., Brunetti, A., Piccinini, M., Malgosa, A., Napolitano, E., Enzo, S., 2011. A multi-technique approach by XRD, XRF, FT-IR to characterize the diagenesis of dinosaur bones from Spain. *Palaeogeography, Palaeoclimatology, Palaeoecology* 310, 92–107.
- Poppe, L.J., Paskerevich, V.F., Hathaway, J.C., Blackwood, D.S., 2001. A laboratory manual for x-ray powder diffraction. *US Geological Survey Open-File Report* 01–041 (88 pp.).
- Potter, P.E., Maynard, J.B., Depetris, P.J., 2005. *Mud and Mudstones, Introduction and Overview*. Springer, Berlin (297 pp.).
- Raven, M.D., Self, P.G., 2017. Outcomes of 12 years of the Reynolds Cup quantitative mineral analysis round robin. *Clays and Clay Minerals* 65, 122–134.
- Roen, J.B., Hosterman, J.W., 1982. Misuse of the term "bentonite" for ash beds of Devonian age in the Appalachian basin. *Geological Society of America Bulletin* 93, 921–925.
- Saupe, F., Vegas, G., 1987. Chemical and mineralogical compositions of black shales (Middle Paleozoic of the Central Pyrenees, Haute-Garonne, France). *Mineralogical Magazine* 51, 357–369.
- Schorin, H., Carias, O., 1987. Analysis of natural and beneficiated ferruginous bauxites by both x-ray diffraction and x-ray fluorescence. *Chemical Geology* 60, 199–204.
- da Silva, A.L., de Oliveira, A.H., Fernandes, M.L.S., 2011. Influence of preferred orientation of mineral in the mineralogical identification process by x-ray diffraction. *International Nuclear Atlantic Conference-INAC 2011 Proceedings*. Associacao Brasileira de Energia Nuclear (11 pp.).
- Soeder, D.J., Enomoto, C.B., Cermak, J.A., 2014. The Devonian Marcellus Shale and Millboro Shale. In: Bailey, C.M., Coiner, L.V. (Eds.), *Elevating Geoscience in the Southeastern United States: New Ideas about Old Terranes-Field Guides for the GSA Southeastern*

- Section Meeting, Blacksburg, Virginia, 2014. The Geological Society of America Field Guide 35, pp. 129–160.
- Srodon, J., Drits, V.A., McCarty, D.K., Hsieh, J.C.C., Eberl, D.D., 2001. Quantitative x-ray diffraction analysis of clay-bearing rocks from random preparations. *Clay and Clay Minerals* 49, 514–528.
- Ver Straeten, C.A., 2004. K-bentonites, volcanic ash preservation, and implications for Early to Middle Devonian volcanism in the Acadian orogen, eastern North America. *Geological Society of America Bulletin* 116, 474–489.
- Ver Straeten, C.A., 2010. Lessons from the foreland basin: Northern Appalachian basin perspectives on the Acadian orogeny. In: Tollo, R.P., Bartholomew, M.J., Hibbard, J.P., Karabinos, P.M. (Eds.), *From Rodinia to Pangea: The Lithotectonic Record of the Appalachian Region*. The Geological Society of America Memoir 206, pp. 251–282.
- Wang, G., Carr, T.R., 2013. Organic-rich Marcellus Shale lithofacies modeling and distribution pattern analysis in the Appalachian Basin. *American Association of Petroleum Geologists Bulletin* 97, 2173–2205.
- Yu, W., 2015. Developments in modeling and optimization of production in unconventional oil and gas reservoirs. (Ph.D. Dissertation). University of Texas at Austin, Austin, Texas, USA (264 pp.).
- Zhou, C.H., Keeling, J., 2013. Fundamental and applied research on clay minerals: from climate and environment to nanotechnology. *Applied Clay Science* 74, 3–9.
- Zwicky, C.N., Lienemann, P., 2004. Quantitative or semi-quantitative? Laboratory-based WD-XRF versus portable ED-XRF spectrometer: results obtained from measurements on nickel-base alloys. *X-Ray Spectrometry* 33, 294–300.